Supporting Information

Protective Buffer Layer Engineering for Sputter-Resistant Transparent Perovskite Solar Cells with Improved Transmission and Efficiency

Abhijit Singha,[1#] Ananta Paul,[2#] Subir Manna,[3] Chinmaya Kumar Sahoo,[4] Vishnu Kumar,[3] Anil Kottantharayil,[5] Sudhanshu Mallick,[2] K. R. Balasubramaniam,[1]* Dinesh Kabra[3]*

[1]Department of Energy Science and Engineering, Indian Institute of Technology Bombay, Mumbai, 400076, India

[2]Department of Metallurgical Engineering and Material Science, Indian Institute of Technology Bombay, Mumbai, 400076, India

[3]Department of Physics, Indian Institute of Technology Bombay, Powai, Mumbai 400076,India.

[4]Centre for Research in Nanotechnology and Science, Indian Institute of Technology Bombay, Powai, Mumbai 400076,India.

[5]Department of Electrical Engineering, Indian Institute of Technology Bombay, Powai, Mumbai 400076,India.

[#]These authors contributed equally to this work.

*Corresponding authors – bala.ramanathan@ese.iitb.ac.in, dkabra@iitb.ac.in

This file includes:

Experimental section

Characterization techniques

Figure S1 to S15

Table S1 to S8

1. EXPERIMENTAL SECTION

1.1 Transparent PSCs fabrication method:

The NIR-TPSCs are fabricated on commercial FTO-coated glass substrates (Pilkington:22 Ω/sq). The cleaning process of the FTO substrate is a crucial step in the overall device fabrication procedure. The substrate is cut into 15 × 15 mm^2 dimensions and etched using a mixture of Zn dust (Sigma-Aldrich) and HCl solution (Sigma-Aldrich). Subsequently, we meticulously clean the FTO glass substrate by immersing it sequentially cleaned in an ultrasonic bath with various solutions: soap water, DI water, acetone, and finally ethanol (Sigma-Aldrich), with each solution treatment lasting for 15 minutes. Subsequently, the thoroughly cleaned FTO substrates are placed in an oven and baked at 150°C for 120 minutes. At this point, the substrates are prepared for the fabrication of devices. The planar SnO_2 precursor solution is prepared by dissolving 0.05 M $SnCl_4 \cdot 5H_2O$ in isopropanol (IPA), followed by stirring for 2 hours. The colloidal SnO_2 solution is obtained by diluting a commercial SnO_2 nanoparticle dispersion in deionized (DI) water at a volume ratio of 1:3. Prior to depositing a bilayer ETL consisting of planar SnO_2 (Sigma-Aldrich) and colloidal SnO_2 (Alfa Aesar), the pristine FTO substrates undergo a 30-minute UV–ozone treatment. A 50 µl layer of planar SnO_2 is spin-coated onto the FTO substrates at 3000 rpm for 30 seconds, followed by annealing at 180°C for 60 minutes. Following cooling to room temperature, a layer of SnO_2 nanoparticles is applied onto the planar SnO_2 at 4000 rpm for 30 seconds and subsequently annealed at 150°C for 30 minutes. To enhance the adhesion of the perovskite to the SnO_2 layer, the SnO_2-coated substrate underwent UV ozone treatment for 30 minutes.

The perovskite precursor solution is prepared by dissolving 1.1 M PbI_2 (TCI Chemicals), 1 M FAI (Gratecell Solar), 0.2 M MABr (Gratecell Solar), and 0.2 M $PbBr_2$ (TCI Chemicals) in DMF (Sigma-Aldrich) and DMSO (Sigma-Aldrich) at a volumetric ratio of 4:1, followed by stirring for 2 hours. After stirring 52 µl of CsI (TCI Chemicals) is added into 1ml of perovskite solution from the stock solution of 1.5 CsI in DMSO and again kept for stirring. Later, the triple cation perovskite is deposited on the SnO_2 coated substrate by spin coating at 2000 rpm for 10s and followed by 6000 rpm for 30s. To ensure first crystallization and uniform film quality, 200 µL of chlorobenzene is dropped dynamically at the centre of the substrate 15 s prior to the end of the second spin. After depositing the perovskite layer, the substrates are annealed at 100 °C for 50 min for crystallization.

For the hole-transport layer (HTL), a mixture of 80 mg Spiro-OMeTAD (Luminescence Technology Corp) dissolved in 1 mL chlorobenzene (Sigma-Aldrich), along with 24 µL of a stock solution containing 520 mg Li-TFSI (bis(trifluoromethane)sulfonamide lithium salt) (Sigma-Aldrich) in 1 mL acetonitrile (Sigma-Aldrich), and 40 µL 4-tert-butylpyridine is used. The Spiro-OMeTAD precursor solution is stored in a nitrogen-filled glovebox for 3 hours before utilization. This doped Spiro-OMeTAD solution is stirred for 10 minutes before use. Subsequently, 50 µL of the Spiro-MeOTAD solution is dynamically spin-coated onto the perovskite substrate at 4000 rpm for 30 seconds. Additionally, we have also deposited an ultrathin layer of KCl and Al_2O_3 between ETL/perovskite and

HTL/perovskite *via* solution and atomic layer deposition (ALD) techniques, respectively.

The metal oxides are deposited via thermal evaporation at a base pressure of < 4×10^{-6} with a deposition rate of 0.1 nm/s. We have used a custom-built RF sputtering system to deposit the rear TE IZO at room temperature. In this work, we use a 2" IZO target (In_2O_3/ZnO = 85:15 wt%). The optimized IZO deposited at room temperature (25 °C) and a chamber pressure of 1.7×10^{-2} mbar used. A shadow mask featuring 27 openings, each measuring 7 mm × 2.5 mm, is employed to delineate three individual cells on each substrate. We have used different sputter power variations to fabricate damage-free transparent PSCs. The deposition rate also varies from ~0.025 to ~0.05 nm/s. We have introduced the Ag bus bar and fingers for better charge collection from the top electrode. A 250 nm Ag layer is deposited by a thermal evaporator at a high vacuum (4×10^{-6} mbar) on the IZO (Testbourne Ltd). Finally, to reduce the reflection loss from the device's top surface, a 110 nm MgF_2 ARC coating (Sigma-Aldrich) is deposited via a thermal evaporator.

Note 1:

According to Kirchhoff's radiation law and Würfel's generalized Planck law, the relationship between PLI and quasi-Fermi level splitting (ΔEF) can be expressed as:[31,32]

$$PLI = \frac{2\pi}{h^3c^2}\frac{E^2a(E)}{exp\left(\frac{E-\Delta E_F}{kT}\right)_{-1}} \quad \ldots\ldots\ldots (3)$$

where E represents the photon energy; T is temperature. α, c, h, and k correspond to absorptivity, speed of light, Planck constant, and Boltzmann constant, respectively. By rearranging this equation, we obtain $PLI \propto \exp(\Delta E_F)$ meaning that the PL intensity is exponentially proportional to the quasi-Fermi level splitting ΔE_F. Since the ΔE_F is directly related to the V_{OC} of the device, and we can express:[33]

$$PLI \propto \exp\left(\frac{qV}{kT}\right) \quad \ldots\ldots\ldots (4)$$

Another way to write this equation is:[34]

$$PLI \propto J_{rad} = J_{0,rad}exp\left(\frac{\Delta E_F}{kT}\right) \quad \ldots\ldots\ldots (5)$$

1.2 Characterizations

Photovoltaic measurements are conducted at room temperature. The $J-V$ characteristics are measure using a Keithley 4200 SCS and 2400 and an LED solar simulator (LSH-7320). Before completing the $J-V$ measurements, the solar simulator is calibrated with one sun illumination under the AM1.5G spectrum using standard Si solar cells supplied by the RERA system (model no RR-86-0). All $J-V$ measurements are performed first in the forward and then in the reverse scan direction with a scan rate of 50-100 mVs^{-1}. A constant voltage is applied to stabilize efficiency, and the current is measured over time at the maximum power point tracking (MPPT). It is crucial to emphasize that the efficiency of the solar cells improved with several measurements until reaching a specific performance level, and the reported results reflect the outcome of the best measurement. Incident Photon-to-Current Efficiency (IPCE or EQE) measurements are conducted to assess the photo response across different wavelengths. The Zolix SCS10-X150 quantum efficiency measurement system is utilized for this purpose. A Zeiss/Ultra 55 scanning electron microscope is employed to analyze the prepared films' surface morphology and examine the device's cross-section, revealing the interfaces. Lifetime measurements are obtained using the Time-Correlated Single Photon Counting (TCSPC) acquisition technique. A pulse-width 60 ps laser diode (Horiba Delta Diode) with an external trigger at a specific repetition rate served as the excitation source (628 nm), delivering a fluence of 5.91 mJ/cm^2. The emitted light is captured by a hybrid picosecond photodetector (HPPD-870) with minimal dark counts. The Instrument Response Function (IRF) is recorded with a milk powder-dispersed solution in a cuvette, achieving a time resolution of approximately 150 ps. The Transient Photo Voltage (TPV) is determined utilizing a 490 nm TOPTICA diode laser, THORLABS white lamp with serial number M00304198, Arb Studio 1104, and a digital oscilloscope, Tektronix DPO 4104B. A PerkinElmer LAMBDA 950 spectrometer is employed to acquire optical absorption, transmittance, and reflection spectra with a step size of 5 nm. The experimental determination of the optical constants, specifically the refractive index (n) and extinction coefficient (k), is conducted using spectroscopic ellipsometry (SE 800). The thickness of IZO layers is measured using the Bruker DektakXT profilometer. The PL images are captured *via* a custom-built setup with a uniform LED-based excitation source and a commercial silicon CCD-based Sensovation camera (Cool Samba HR-830) detector. The samples are fabricated following the same procedure as the full device fabrication, but only up to the buffer layer (~10 nm). The LED excitation source consists of two LED arrays with a central wavelength of ~630 nm. The integration time is 500 ms. The pixel resolution of the detector is 3324 × 2504 with a pixel size of 5.4 μm. A 680 nm long filter is also employed during the image capture. Further, the images are refined using custom Python-based programming. The thickness of the MOs is measured using a quartz crystal microbalance (QCM) and a thickness monitor integrated with the thermal evaporator, with external calibration of tooling performed using a Dektak profilometer. Optical transmission was evaluated by depositing the films onto glass substrates at a fixed thickness of ~10 nm.

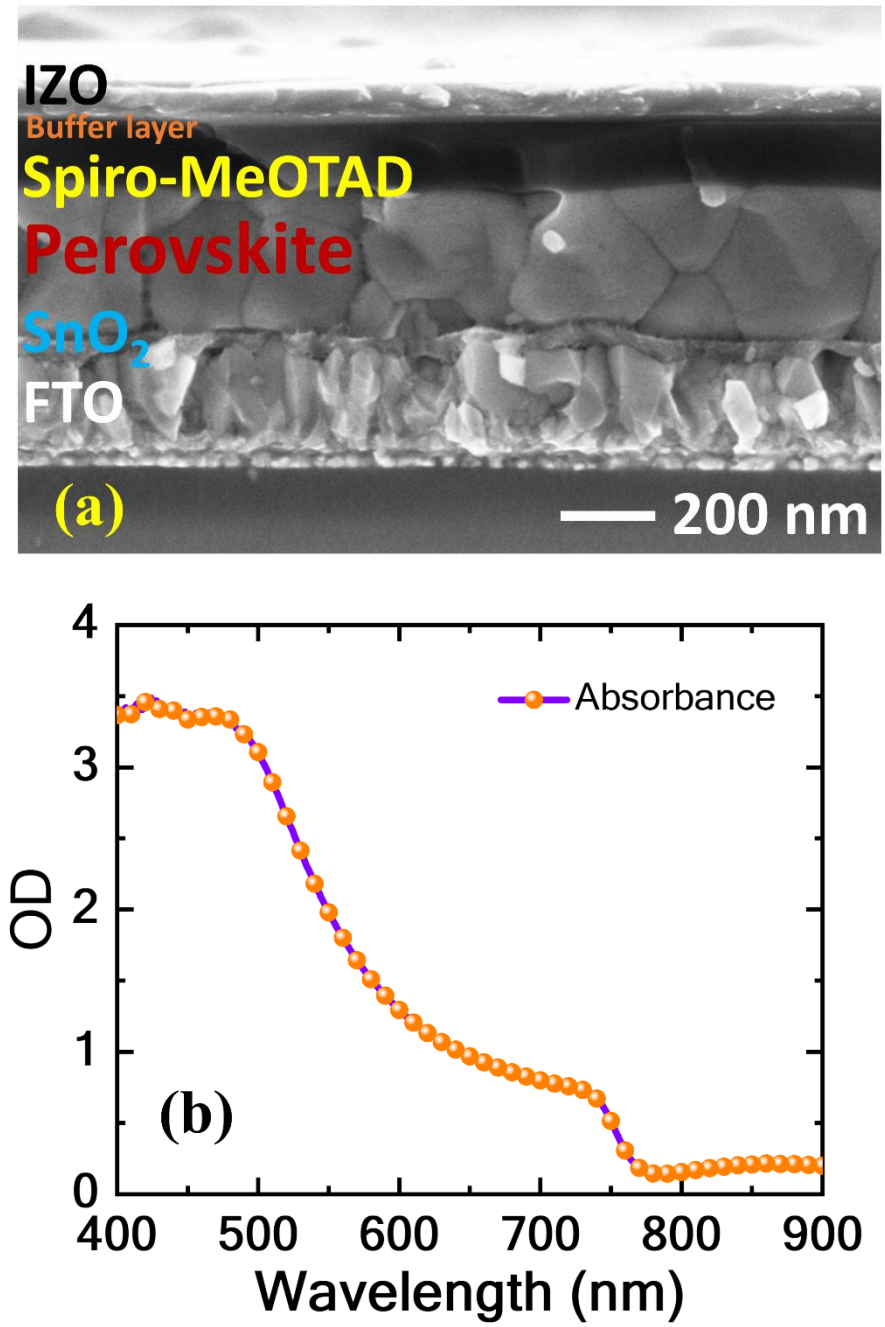

Figure S1: (a) Cross-sectional field emission scanning electron microscopy analysis image of the layered structured transparent PSCs, and (b) Absorption analysis of the perovskite photo absorber layer.

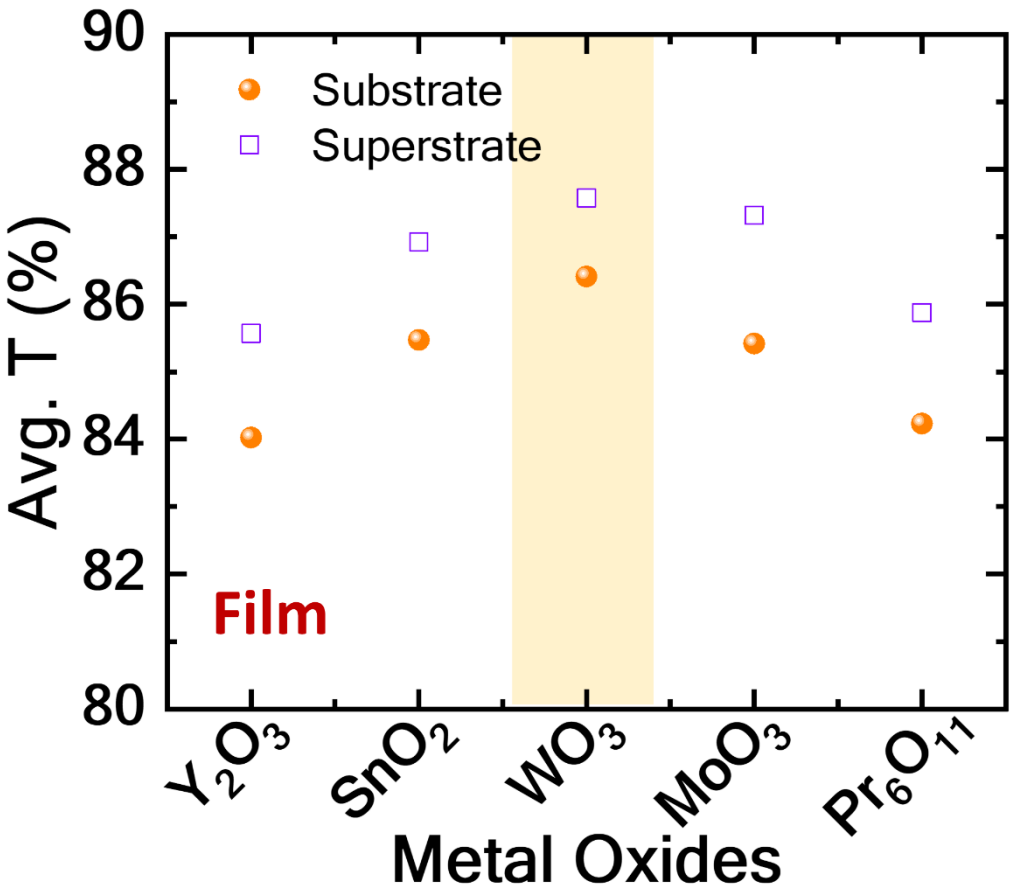

Figure S2: Variation of the average transmission of the metal oxide thin films while illuminating from the substrate (4T) and superstrate (2T), respectively. Among all of them, WO_3 provides the highest average transmission in both cases.

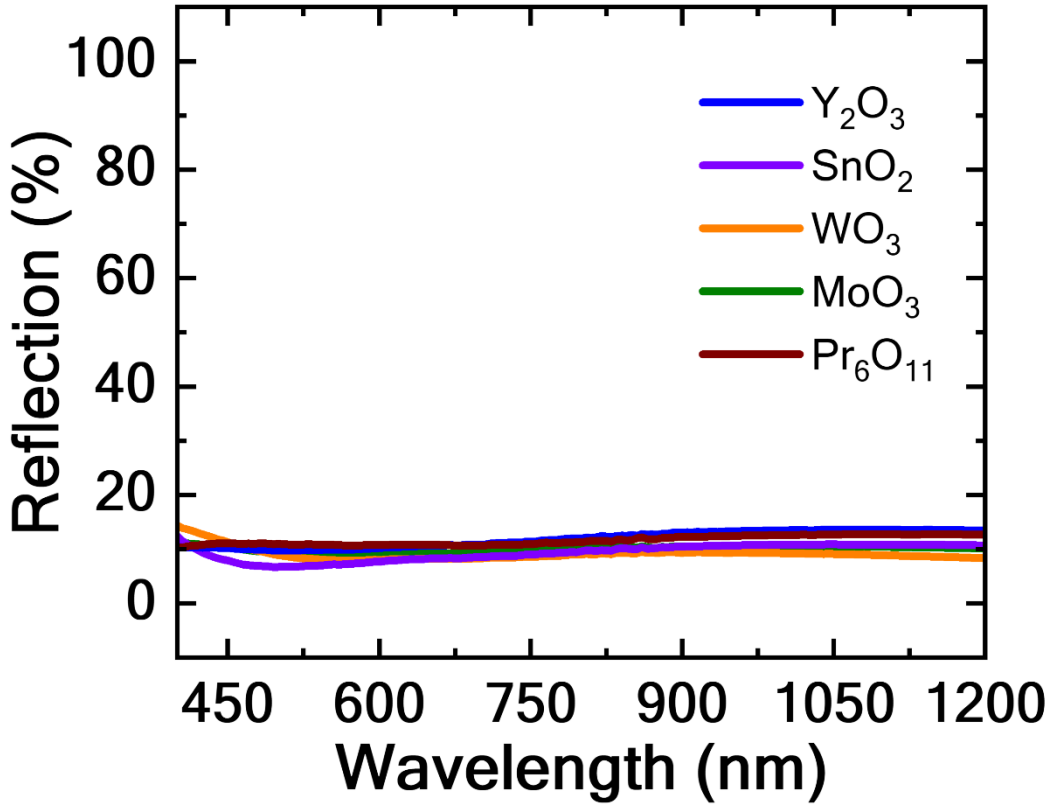

Figure S3: Reflection spectra of the different MOs thin films

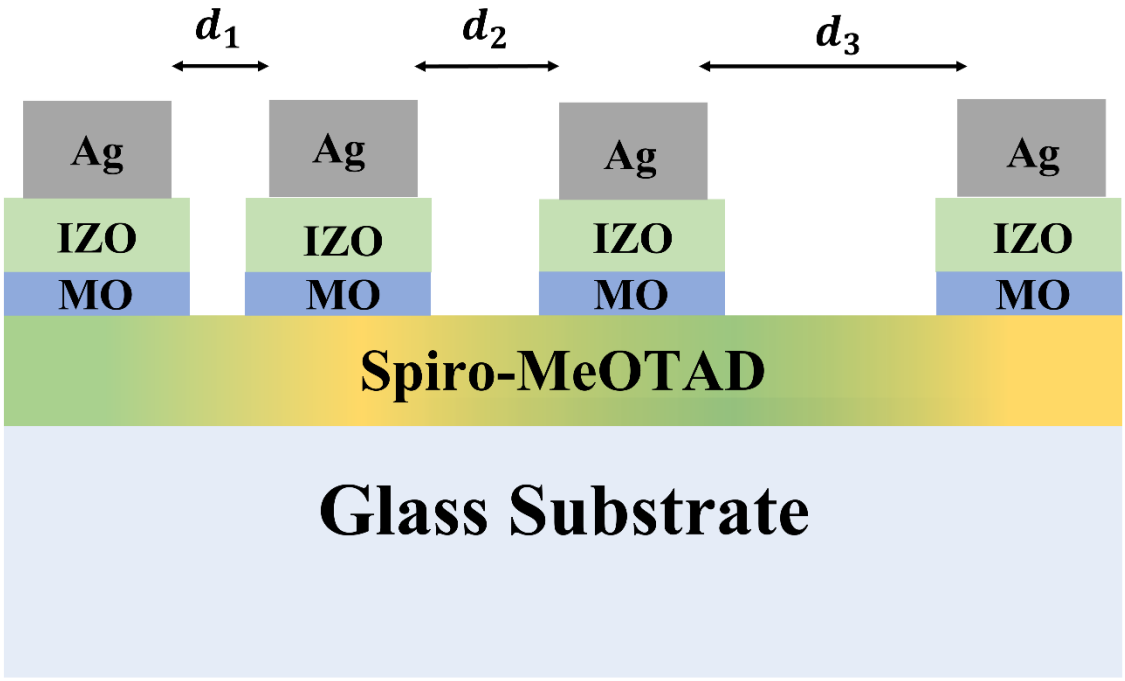

Figure S4: Side view of the device architecture used for TLM analysis.

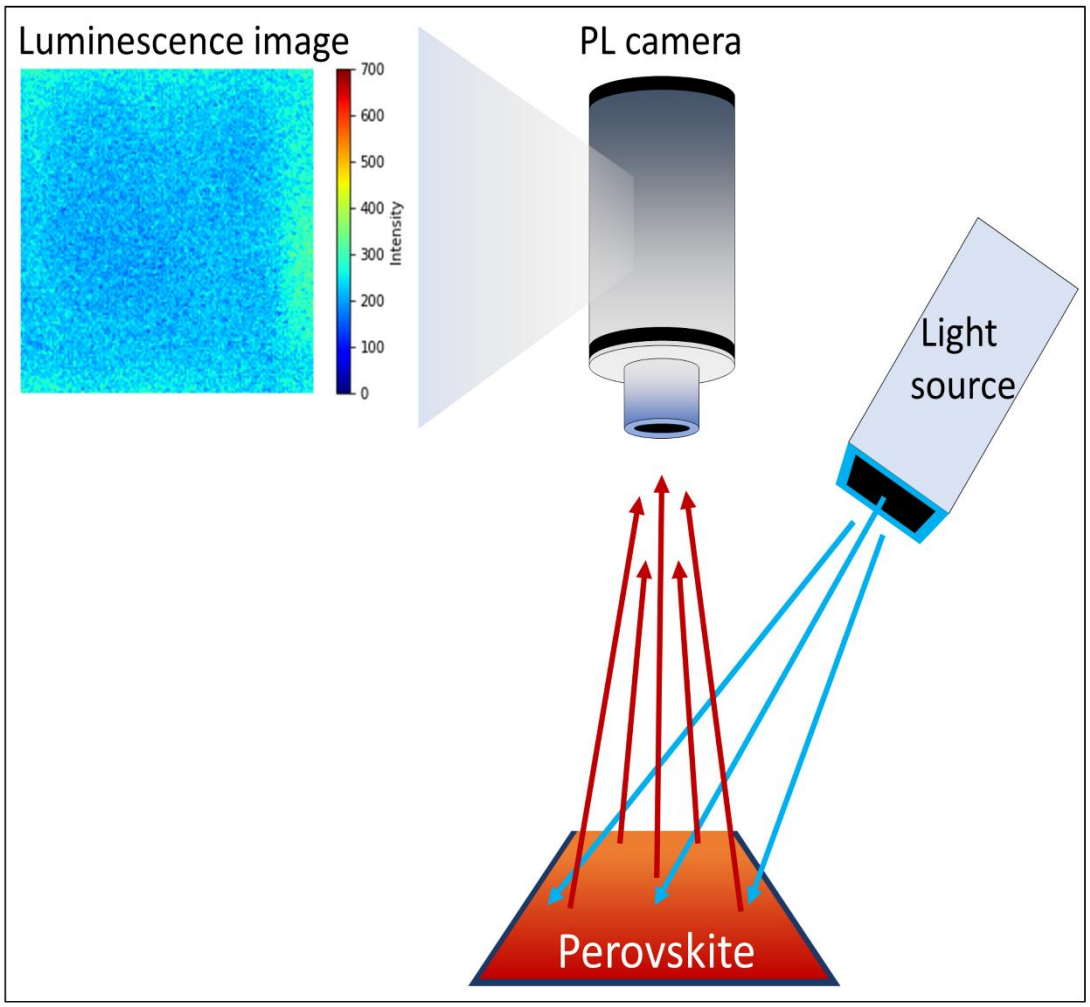

Figure S5: Schematic representation of PL imaging setup.

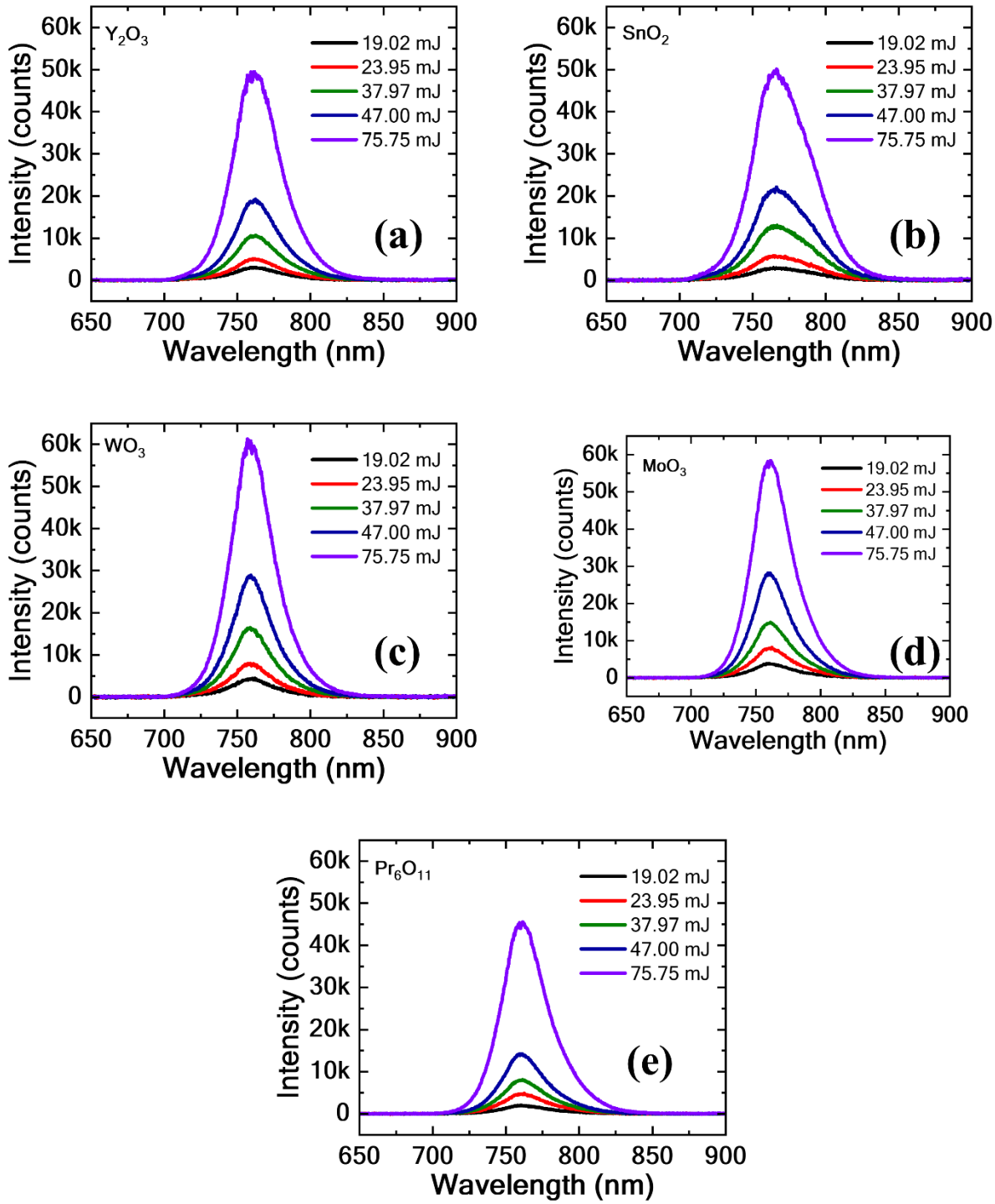

Figure S6: Gaussian distributions of the PL analysis of perovskite thin films incorporated with various metal oxide thin films at varying fluence.

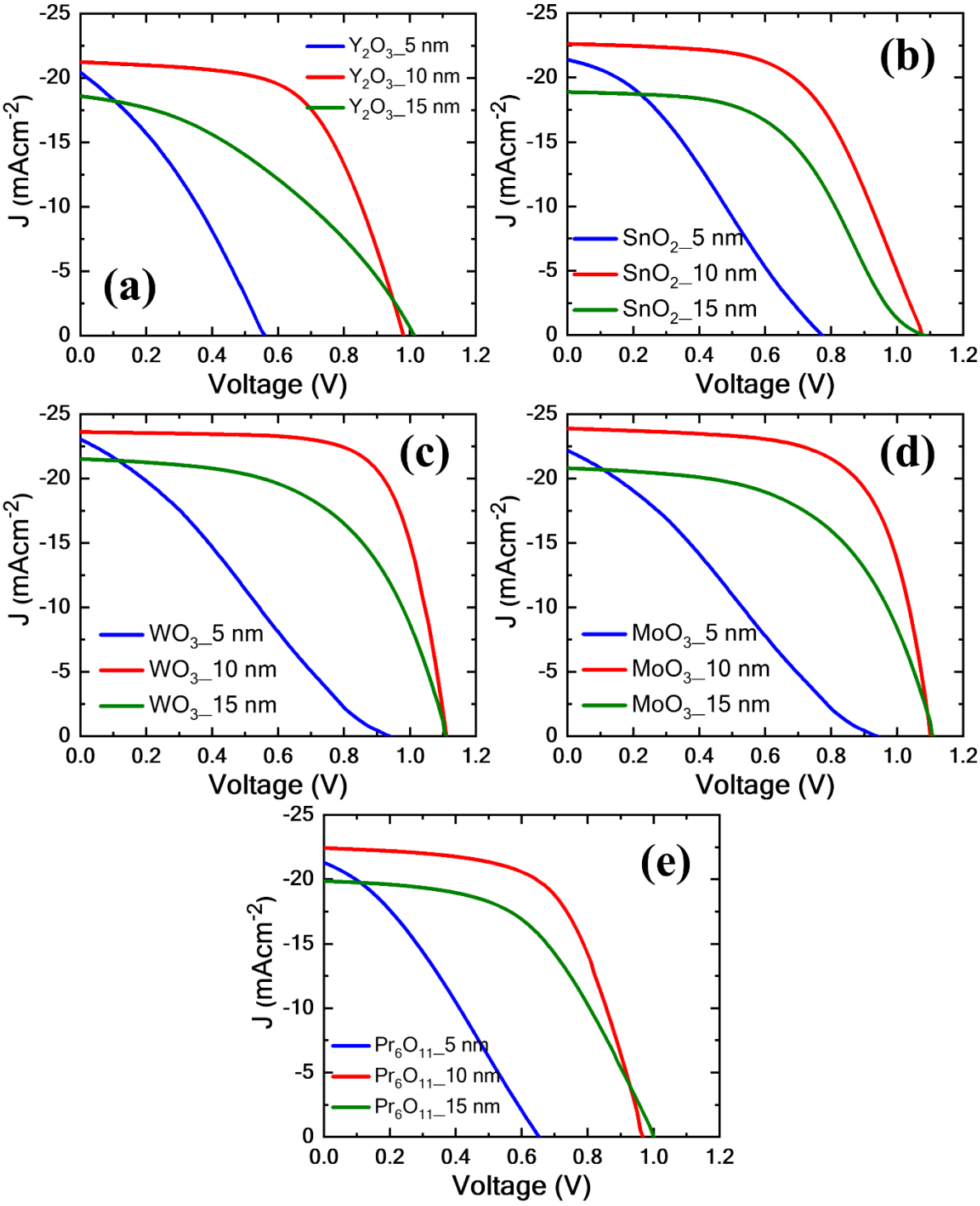

Figure S7: $J-V$ characteristics of the transparent PSCs incorporated with various metal oxides having varying metal oxide thickness. In all the cases the 5 nm metal oxide thickness resulted in '*S*' shaped characteristics which is known as shunted $J-V$ appears due to sputter damage. On the other hand, the devices with 15 nm thick MOs possess lower J_{SC} and FF due to increased parasitic resistance. The 10 nm thickness of metal oxide is the most optimal thickness for the application in *n-i-p* transparent perovskite solar cell development.

Table S1: $J-V$ parameters of the transparent PSCs with varying MOs thicknesses (5 and 15 nm) under bottom-side illumination conditions.

MOs	Thickness (nm)	J_{SC} (mA cm^{-2})	V_{OC} (V)	FF (%)	PCE (%)
Y_2O_3	5	20.24	0.56	24.07	2.74
	15	18.52	1.0	41.74	7.73
SnO_2	5	21.38	0.772	27.07	4.40
	15	18.87	1.085	49.82	10.20
WO_3	5	22.91	0.93	25.72	5.47
	15	21.50	1.105	53.48	12.71
MoO_3	5	22.16	0.947	26.77	5.61
	15	20.76	1.105	55.3	13.84
Pr_6O_{11}	5	21.31	0.65	27.07	3.74
	15	19.85	1.0	54.73	10.86

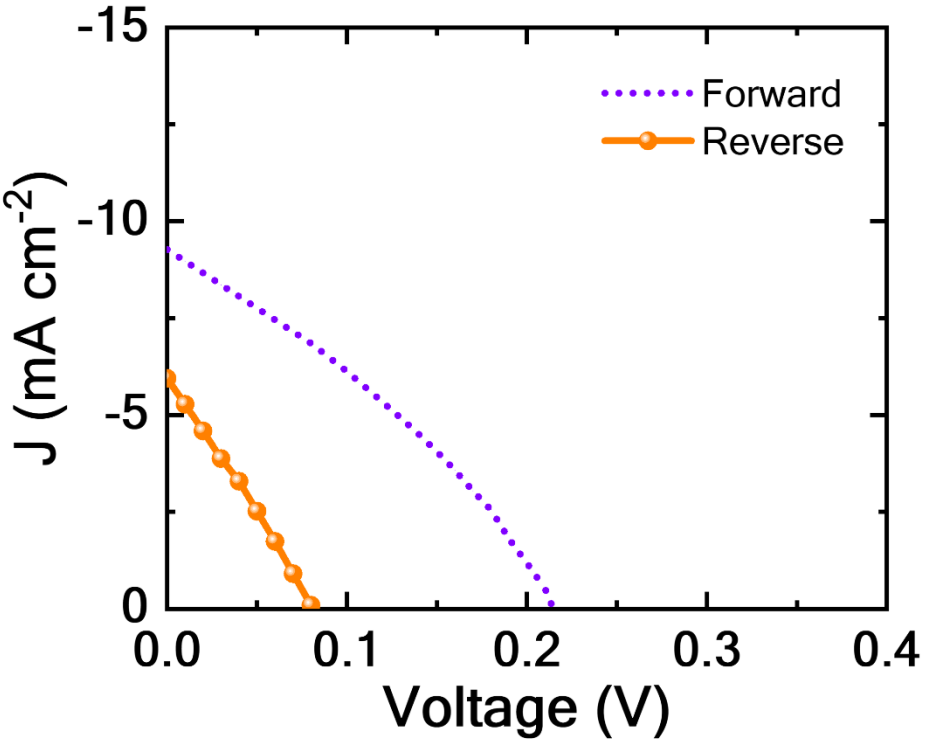

Figure S8: $J-V$ characteristics of the transparent PSCs without a buffer layer.

Table S2: Photovoltaic ($J-V$) parameters of the transparent PSCs without a buffer layer

Device	Scan	J_{SC} (mA cm^{-2})	V_{OC} (V)	FF (%)	PCE (%)
Transparent	FS	9.27	0.22	63.9	0.31
PSC_W/o buffer	RS	5.95	0.08	13.2	0.27

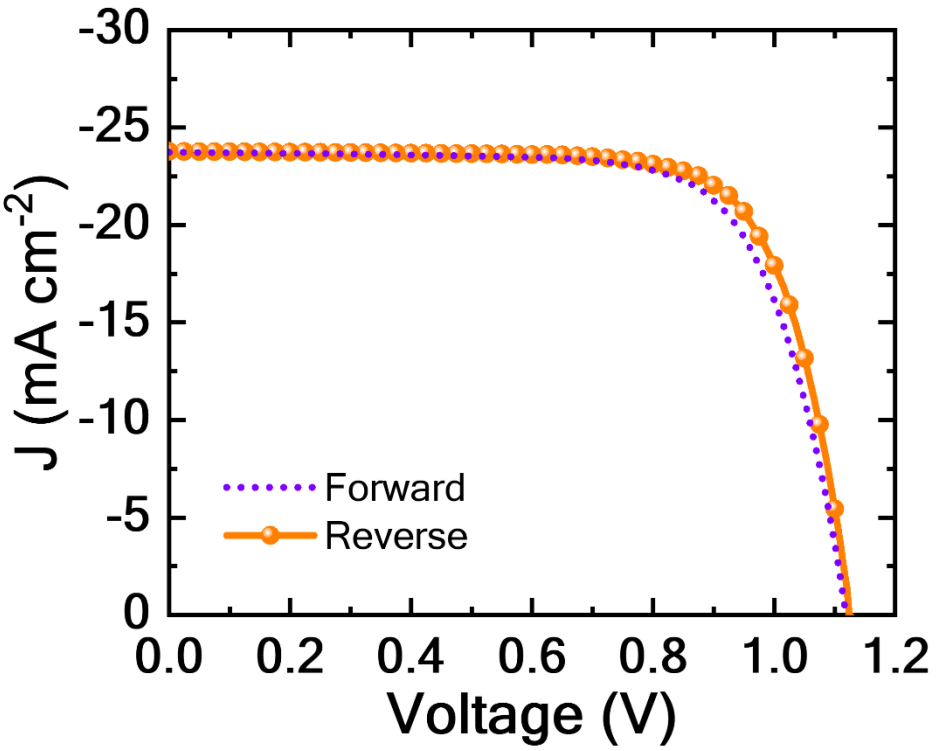

Figure S9: $J-V$ characteristics of the opaque perovskite solar cells employing a bi-layer Au/Ag counter electrode are presented. The Au/Ag combination was selected solely to reduce the use of gold, without any additional functional considerations.

Table S3: Photovoltaic ($J-V$) parameters of the opaque PSCs

Device	Scan	J_{SC} (mA cm^{-2})	V_{OC} (V)	FF (%)	PCE (%)
Opaque PSC	FS	23.74	1.12	72.1	19.2
	RS	23.78	1.13	74.4	20.0

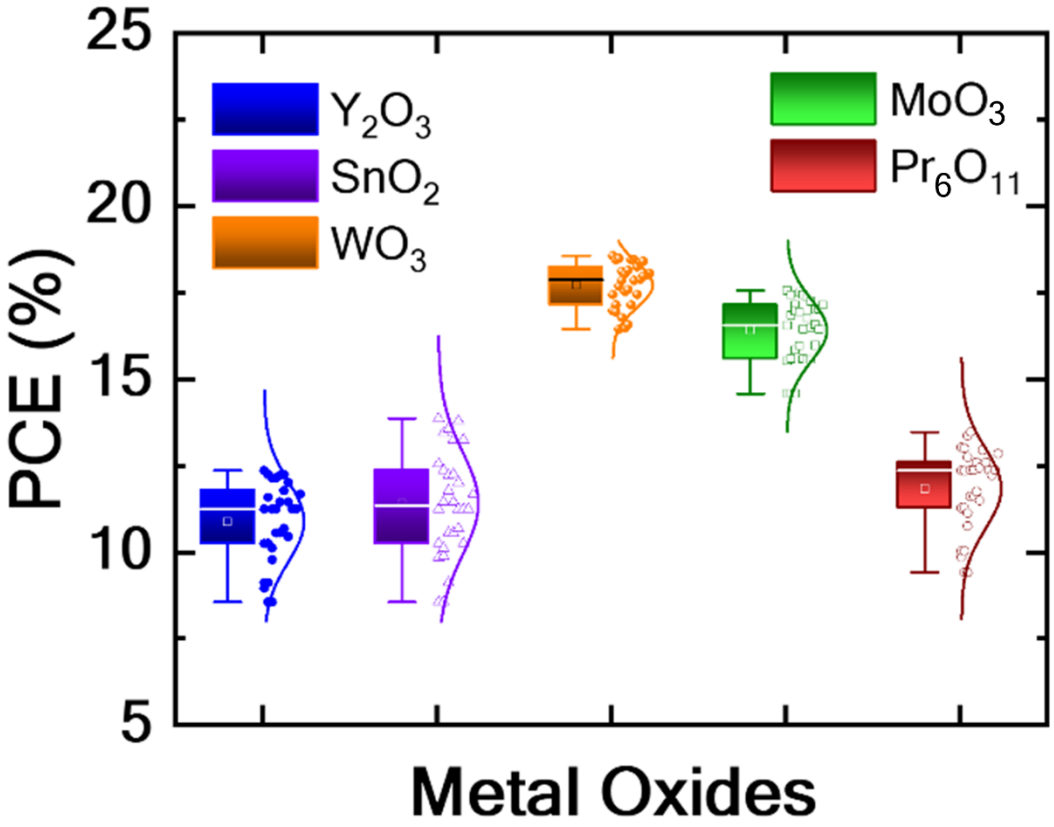

Figure S10: Statistical distribution performed on more than 30 devices of the transparent PSCs having different MOs. The *d*-block MO-based transparent PSCs provide higher photovoltaic performance, while the PSCs with a WO_3 buffer layer possess the champion PCE.

Table S4: A summary of the $J-V$ parameters and active area of the state-of-the-art transparent PSCs having *n-i-p* architecture from 2020.

Year	Perovskite	Active area (cm^2)	J_{SC} (mA cm^{-2})	V_{OC} (V)	FF (%)	PCE (%)	Ref
2020	$FA_{0.83}Cs_{0.17}Pb(I_{1-y}Br_y)_3$	0.056	19.7	1.16	78.7	18.0	1
2020	$Rb_{0.05}Cs_{0.095}MA_{0.1425}FA_{0.7125}PbI_2Br$	0.21	18.0	1.205	78.9	17.1	2
2022	$(FAPbI_3)_{0.95}(MAPbBr_3)_{0.05}$	-	23.32	1.07	74.5	18.59	3
2022	$FA_{0.83}Cs_{0.17}Pb(I_{0.7}Br_{0.3})_3$	0.16	18.35	1.193	70.0	15.42	4
2023	$Cs_{0.05}(FA_{0.83}MA_{0.17})_{0.95}Pb(I_{0.83}Br_{0.17})_3$	0.09	20.11	0.993	73.17	14.78	5
2023	$FA_{0.65}MA_{0.20}Cs_{0.15}Pb(I_{0.8}Br_{0.2})_3$	0.07	21.05	1.181	80.1	19.89	6
2023	$FA_{0.65}MA_{0.20}Cs_{0.15}Pb(I_{0.8}Br_{0.2})_3$	0.09	20.29	1.217	77.59	19.15	7
2024	$(FAPbI_3)_{0.85}(MAPbBr_3)_{0.15}$	0.058	19.83	1.042	75.39	15.58	8
2025	$Cs_{0.05}(FA_{0.95}MA_{0.05})_{0.95}Pb(I_{0.95}Br_{0.05})_3$	0.05	21.37	1.11	60.83	14.52	9
2025	$MA_{0.10}Cs_{0.10}FA_{0.80}Pb(I_{0.78}Br_{0.22})_3$	0.52	19.81	1.21	74.89	18.00	10
2025	This study $[Cs_{0.05}(FA_{0.83}MA_{0.17})_{0.95}Pb(I_{0.83}Br_{0.17})_3]$	0.17	23.75	1.12	71.4	19.0	-

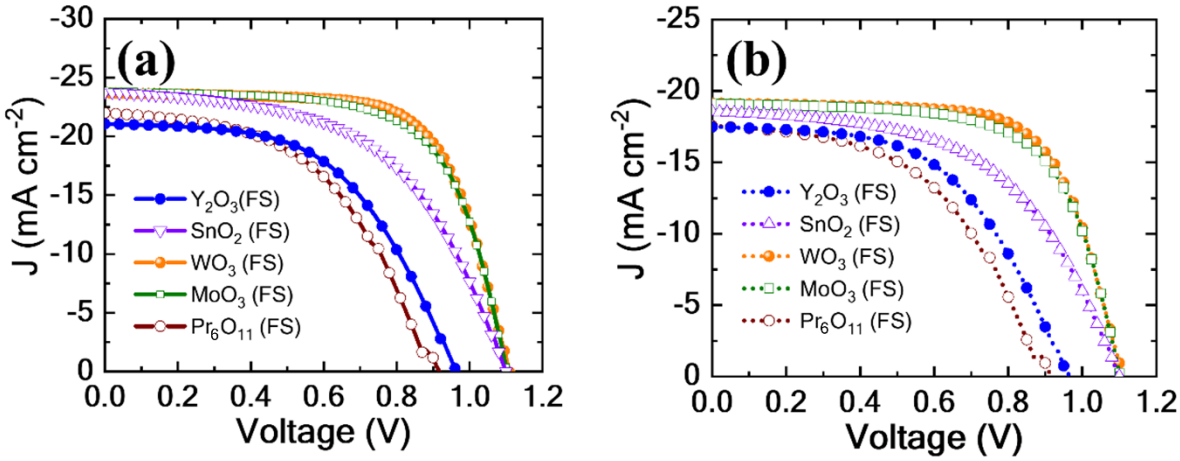

Figure S11: $J-V$ characteristics of the transparent PSCs with different MOs measured under forward scan in **(a)** bottom (Glass/FTO) and **(b)** top (IZO) illumination conditions, respectively.

Table S5: $J-V$ parameters of the transparent PSCs with different MOs measured under forward scan for both bottom and top illumination conditions respectively.

Illumination side	**Device**	**Scan**	J_{sc} **(mA cm^{-2})**	V_{oc} **(V)**	**FF (%)**	**PCE (%)**
Bottom (Glass/FTO)	Y_2O_3	FS	21.06	0.96	53.4	10.8
	SnO_2	FS	22.54	1.07	55.0	13.3
	WO_3	FS	23.69	1.11	68.2	17.9
	MoO_3	FS	23.64	1.10	66.5	17.1
	Pr_6O_{11}	FS	22.00	0.92	49.1	9.9
Top (IZO)	Y_2O_3	FS	17.48	0.96	53.4	8.9
	SnO_2	FS	19.48	1.07	55.0	11.1
	WO_3	FS	19.13	1.11	68.2	14.4
	MoO_3	FS	19.11	1.09	66.5	13.8
	Pr_6O_{11}	FS	17.55	0.95	47.6	7.9

Table S6: Parasitic resistance calculated from $J-V$ characteristics of the transparent PSCs with different MOs.

Device	R_s **(Ω.cm)**	R_{sh}**(Ω.cm)**
Y_2O_3	12.7	803
SnO_2	15.8	1446
WO_3	6.4	3098
MoO_3	7.4	2906
Pr_6O_{11}	10.6	847

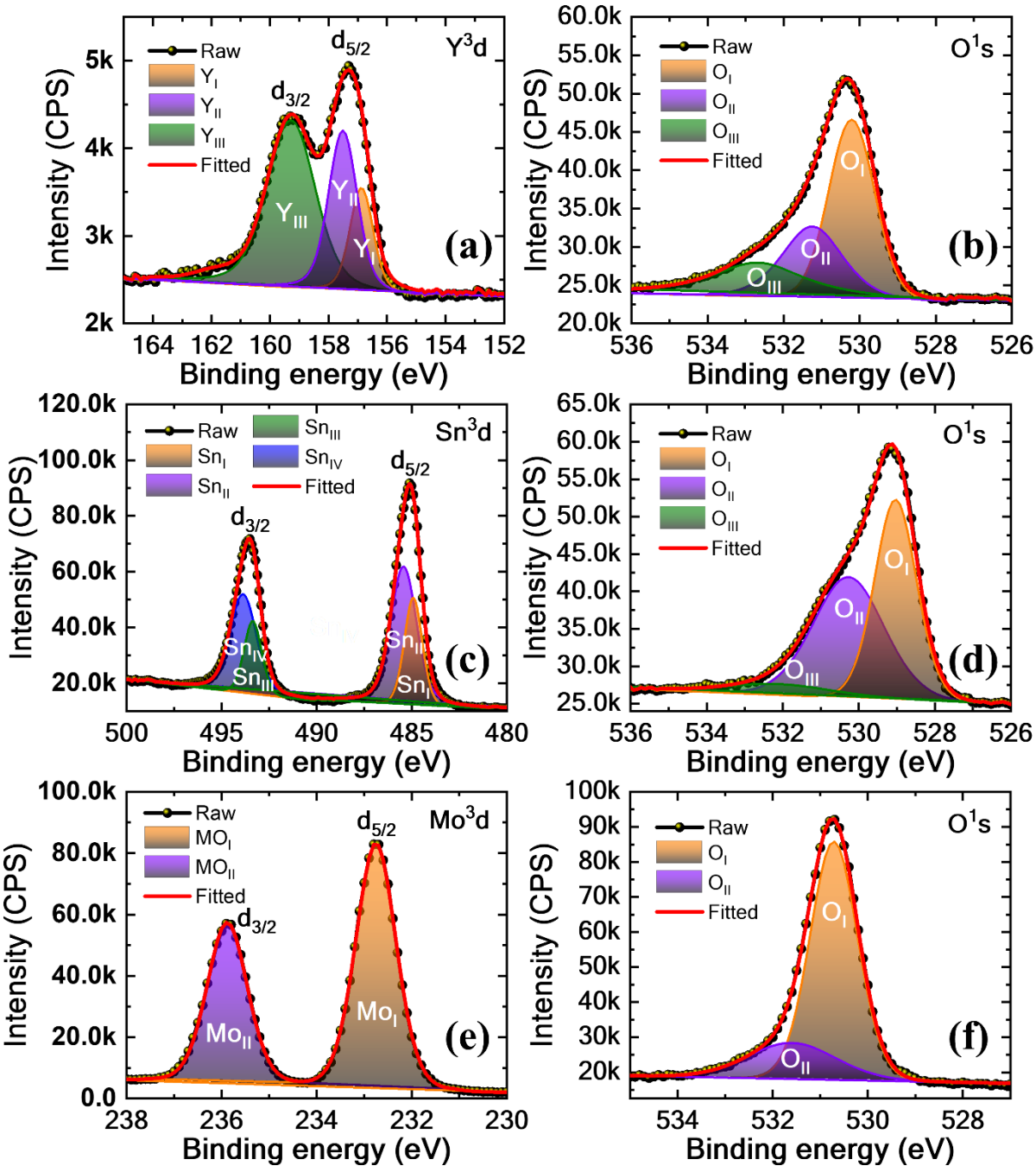
Raw
Y_I
Y_II
Y_III
Fitted
d_5/2
d_3/2
Y^3d
(a)
Intensity (CPS)
Binding energy (eV)
O^1s
O_I
O_II
O_III
(b)
Sn_III
Sn_IV
Sn_I
Sn_II
Sn^3d
(c)
(d)
MO_I
MO_II
Mo^3d
Mo_I
Mo_II
(e)
(f)

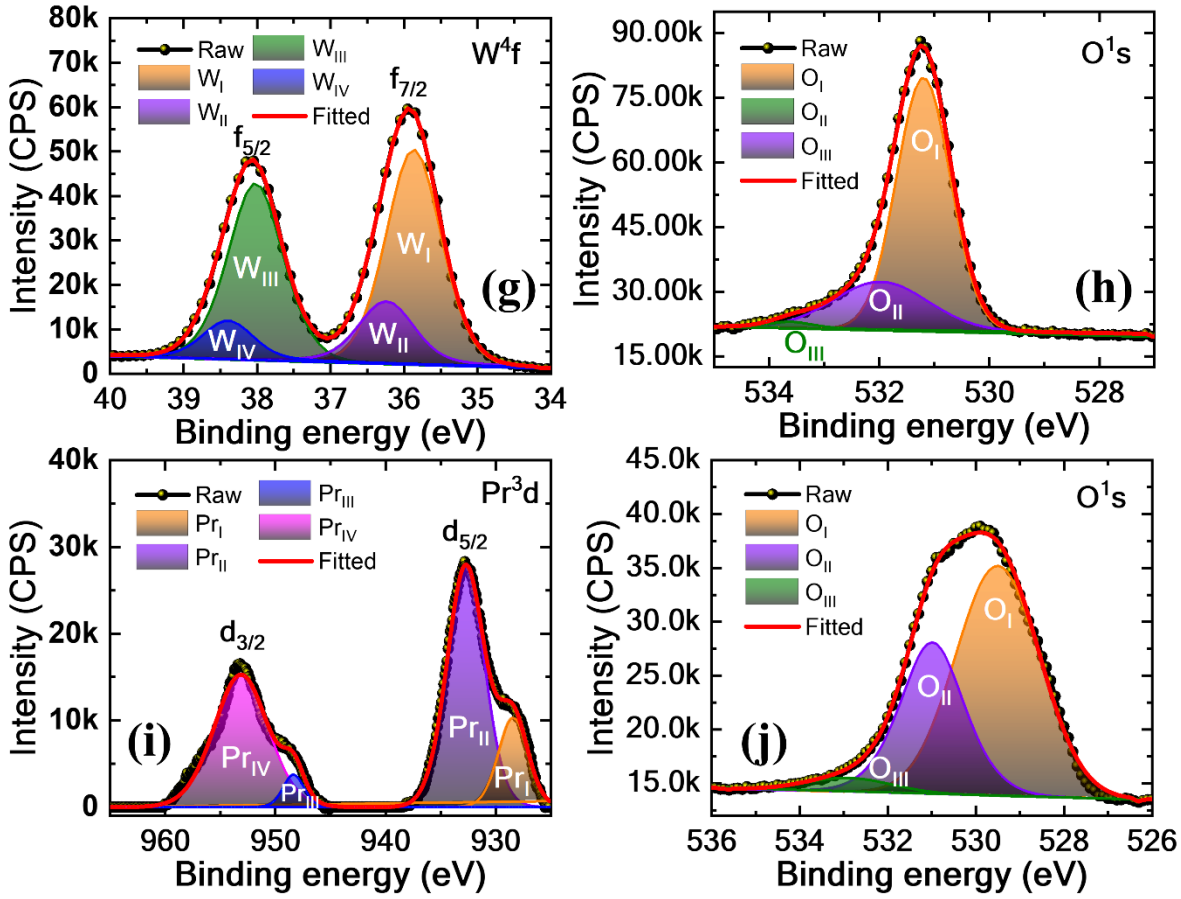

Figure S12: Fitted X-ray photoelectron spectroscopy (XPS) spectra of MOs, showing (a, c, e, g, i) metal core-level spectra and (b, d, f, h, j) corresponding oxygen 1s spectra. The oxygen 1s signals in all cases were deconvoluted into three Gaussian components; the dominant peak corresponds to lattice oxygen (O_I), the intermediate binding energy peak (O_{II}) is attributed to oxygen vacancies (O^{2-}), and the highest binding energy peak (O_{III}) is assigned to surface-adsorbed oxygen species (O^-).

Table S7: Atomic concentrations of the deconvoluted oxygen species in MOs, as determined from XPS analysis.

MO	Peak	Atomic %
Y_2O_3	O_I	50.03
	O_{II}	27.11
	O_{III}	22.86
SnO_2	O_I	46.99
	O_{II}	45.99
	O_{III}	7.02
MoO_3	O_I	65.04
	O_{II}	22.02
	O_{III}	12.95
WO_3	O_I	74.04
	O_{II}	24.40
	O_{III}	1.56
Pr_6O_{11}	O_I	63.12
	O_{II}	32.95
	O_{III}	3.93

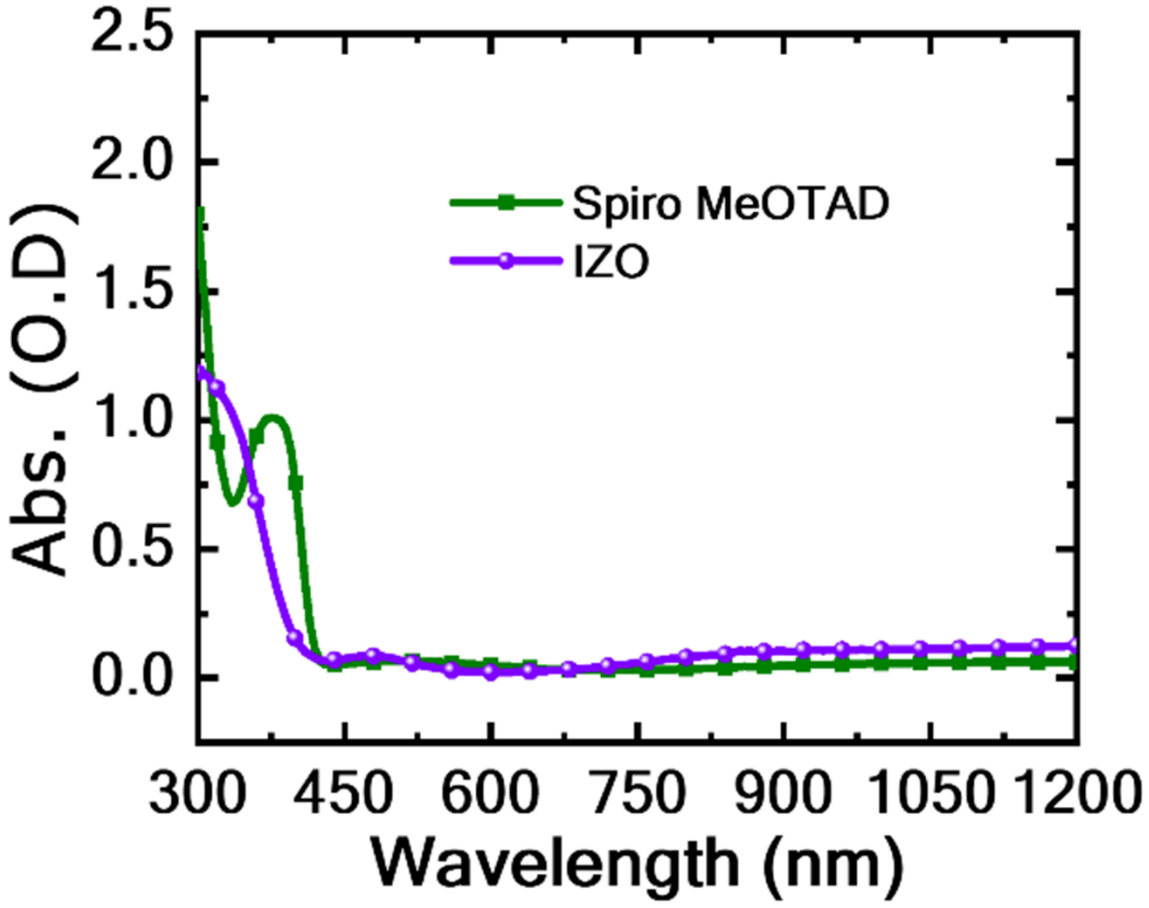

Figure S13: The absorption spectra of the Spiro-MeOTAD HTL and IZO TE. Due to their internal absorption (~400 nm) a loss in the current density is observed for the transparent PSCs while shining from the top (IZO) side.

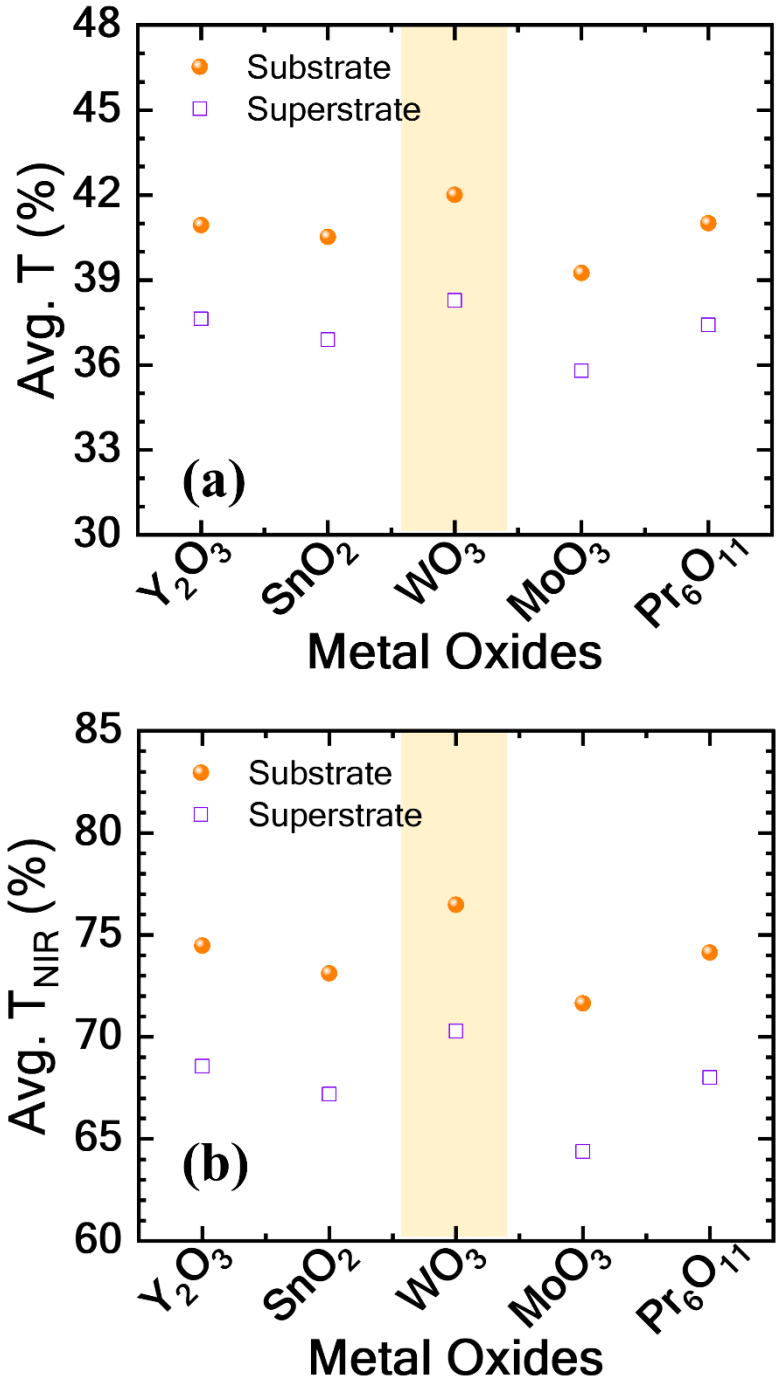

Figure S14: Average transmission of the transparent PSCs incorporated with different MOs at the wavelength range of **(a)** 300-1200 nm and **(b)** 800-1200 nm. In both cases the transparent PSCs incorporated with the WO_3 buffer layer provide the highest average transmission.

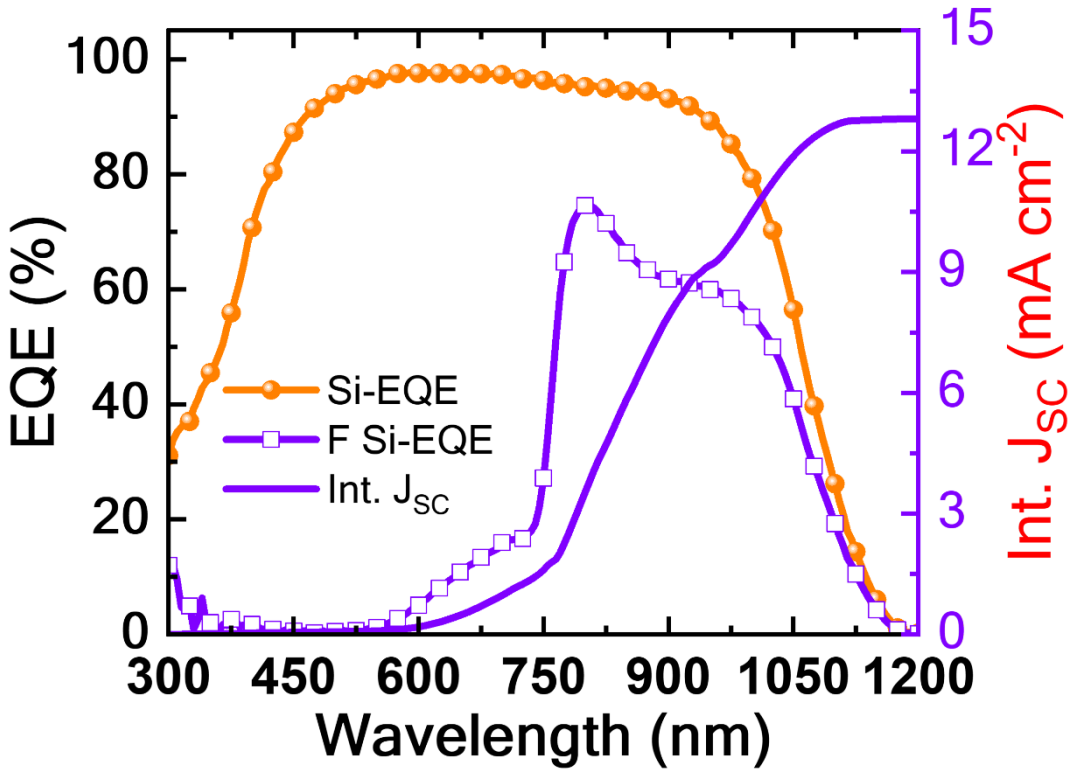

Figure S15: EQE spectrum of standalone passivated emitter rear contact (PERC) Si-solar cells and perovskite filtered EQE with int. J_{SC}, which is used for 4T tandem performance estimation.

Table S8: Estimation of 4T Si/perovskite tandem solar cells performance

Device	J_{SC} (mA cm^{-2})	V_{OC} (V)	FF (%)	PCE (%)
Standalone transparent PSCs	23.75	1.12	71.4	19.0
Standalone Si SC	38.54	0.734	82	23.0
Perovskite filtered Si SC	12.81	0.734	82	7.71
4T Tandem	-	-	-	26.71

References:

1. S. Gharibzadeh, I. M. Hossain, P. Fassl, B. A. Nejand, T. Abzieher, M. Schultes, E. Ahlswede, P. Jackson, M. Powalla, S. Schäfer, M. Rienäcker, T. Wietler, R. Peibst, U. Lemmer, B. S. Richards and U. W. Paetzold, Advanced Functional Materials, 2020, 30, 1909919.
2. T. Duong, H. Pham, T. C. Kho, P. Phang, K. C. Fong, D. Yan, Y. Yin, J. Peng, M. A. Mahmud, S. Gharibzadeh, B. A. Nejand, I. M. Hossain, M. R. Khan, N. Mozaffari, Y. Wu, H. Shen, J. Zheng, H. Mai, W. Liang, C. Samundsett, M. Stocks, K. McIntosh, G. G. Andersson, U. Lemmer, B. S. Richards, U. W. Paetzold, A. Ho-Ballie, Y. Liu, D. Macdonald, A. Blakers, J. Wong-Leung, T. White, K. Weber and K. Catchpole, Advanced Energy Materials, 2020, 10, 1903553.
3. M. J. Jeong, J. H. Lee, C. H. You, S. Y. Kim, S. Lee and J. H. Noh, Advanced Energy Materials, 2022, 12, 2200661.
4. C. Tian, X. Gao, J. Li, J. Pan, G. Yu, B. Huang, Y. Wen, H. Zhu, T. Bu, Y.-B. Cheng and F. Huang, Solar RRL, 2022, 6, 2200134.
5. Z. Yuan, M. Zhang, Z. Yen, M. Feng, X. Jin, A. Ibrahim, M. G. Ahmed, T. Salim, R. A. Gonçalves, T. C. Sum, Y. M. Lam and L. H. Wong, ACS Appl. Mater. Interfaces, 2023, 15, 37629–37639.
6. W. Chai, L. Li, W. Zhu, D. Chen, L. Zhou, H. Xi, J. Zhang, C. Zhang and Y. Hao, Research, 2023, 6, 0196.
7. Z. Li, X. Li, X. Chen, X. Cui, C. Guo, X. Feng, D. Ren, Y. Mo, M. Yang, H. Huang, R. Jia, X. Liu, L. Han, S. Dai and M. Cai, Joule, 2023, 7, 1363–1381.
8. E. Han, J.-H. Yun, I. Maeng, T. Qiu, Y. Zhang, E. Choi, S.-M. Lee, P. Chen, M. Hao, Y. Yang, H. Wang, B. W. Zhang, J. S. Yun, J. Seidel, M. Lyu and L. Wang, Nano Energy, 2024, 131, 110136.
9. B. Shen, Q. Zhou, Q. Sun, B. Kang and S. R. P. Silva, Chemical Engineering Journal, 2025, 513, 163004.
10. X. Cui, X. Li, Z. Wang, Z. Li, X. Chen, J. Tang, X. Feng, S. La, J. Chen, Z. Zhang, Z. Yuan, X. Sun and M. Cai, Device, 2025, 3, 100558.